Afterslip and viscoelastic relaxation model inferred from the large scale postseismic deformation following the 2010 Mw 8.8 Maule earthquake (Chile)

E. Klein[1,2], L. Fleitout[1], C. Vigny[1], J.D. Garaud[3]

[1]*Laboratoire de Géologie, ENS, UMR 8538, CNRS, member of PSL-research university,*

24 rue Lhomond, 75231 Paris Cedex 05, FR

[2] *now at Institut Physique du Globe, UMR 7516, Universit de Strasbourg/EOST, CNRS Strasbourg, FR*

[3]*Onera - The French Aerospace Lab, F-92322 Châtillon, FR*

Supplementary material.

1   ABOUT GPS TIME SERIES ANALYSIS

We provide here the complete list of GPS stations used to define the global reference frame (table S1) of our solution. The complete interseismic velocity field (compiled and interpolated using cubic spline) is presented on (fig.S1). Known velocities come from our own GPS processing, upgraded with published data [Brooks et al.,2003, Ruegg et al., 2009, Moreno et al.,2011].

Fig.S2 sums up the time series analysis process:

a) estimation of the preseismic (interseismic) velocity between the beginning of the time series and 2010,

b) Correction of the time series from the preseismic velocity. The residual velocity before the Maule earthquake is then null and only the postseismic signal remains,

c) Estimation of a global trend using an exponential function (black curve), which helps to minimize the impact of noise and seasonal variations. Finally, estimation of mean velocities over different temporal window.

Table S1. Stations used for the realization of the global reference frame

Station	Lat (°)	Lon (°)	before 2010	after 2010	Station	Lat (°)	Lon (°)	before 2010	after 2010
BRAZ	-15.95	-47.88	X	X	MDO1	30.68	-104.01	X	X
KOUR	5.25	-52.81	X	X	PIE1	34.30	-108.12	X	X
BRFT	-3.88	-38.43	X	X	YELL	62.48	-114.48	X	X
ISPA	-27.12	-109.34	X	X	GOLD	35.42	-116.89	X	X
GLPS	-0.74	-90.30	X	X	DRAO	49.32	-119.63	X	X
SAVO	321.57	-12.94	X	X	FAIR	64.98	-147.50	X	X
TOPL	311.67	-10.17	X	X	KOKB	22.13	-159.66	X	X
MSCG	305.46	-20.44	X	X	CHAT	-43.96	-176.57	X	X
POAL	308.88	-30.07	X	X	AUCK	-36.60	174.83	X	X
CHPI	-22.69	-44.98	X	X	MCM4	-77.84	166.67	X	X
UFPR	-25.45	-49.23	X	X	MAC1	-54.50	158.94	X	X
SANT	-33.15	-70.67	X	-	TIDB	-35.40	148.98	X	X
LPGS	-34.91	-57.93	X	-	HOB2	-42.80	147.44	X	X
RIO2	-53.79	-67.75	X	X	GUAM	13.59	144.87	X	X
VILL	40.44	-3.95	X	X	PERT	-31.80	115.89	X	X
MADR	40.43	-4.25	X	X	IRKT	52.22	104.32	X	X
MASP	27.76	-15.63	X	X	DAV1	-68.58	77.97	X	X
OHIG	-63.32	-57.90	X	X	KERG	-49.35	70.26	X	X
BRMU	32.37	-64.70	X	X	KIT3	39.14	66.88	X	X
THU1	76.54	-68.83	X	X	MATE	40.65	16.70	X	X
AREQ	-16.47	-71.49	X	X	GRAZ	47.07	15.49	X	X
WES2	42.61	-71.49	X	X	POTS	52.38	13.07	X	X
GODE	39.02	-76.83	X	X	ONSA	57.40	11.93	X	X
ALGO	45.96	-78.07	X	X	NYAL	78.93	11.87	X	X

We also provide an additional document (Klein_Suppl_PostVel_Tables.pdf) that compiles the tables of mean velocities (horizontal and vertical) estimated over different time windows over the 5 years of available GPS data after the earthquake (represented on Fig.3 and Fig.5 on the main text) :

- between 0 (day after the Maule earthquake) and 2 months
- between 2 and 6 months after the Maule earthquake
- between 6 months and the 1st year after the Maule earthquake
- between the 1st and the 2nd year after the Maule earthquake
- between the 2nd and the 3rd year after the Maule earthquake

- between the 3rd and the 4th year after the Maule earthquake

Note that the velocity uncertainties account for the dispersion between the global trend and the data at the time of velocities estimation. Those uncertainties are then very sensitive to the seasonal variations.

2   FE MODEL

We detail here the parametrization of the 3D FE mesh. It is composed of 252 186 4-nodes 3D-tetrahedral elements, for a total of 46587 nodes. The resolution of the mesh is obtained from a convergence study and the refinement consists of a factor 35 between the size of the smallest elements along the slab, which base measures less than $2000 km^2$ (side of about 20 km), and the biggest elements on the edge of the mesh, which base measures about $68000 km^2$ (side of more than 350 km). The refinement function is applied linearly as function of distance from the trench. The extension of the mesh is of $60°$ in longitude eastward from the trench, westward from the eastern coast of Argentina. Practically, it spans a geometry between $10°$S and $60°$S and between $255°$N and $340°$N, thus encompassing the whole South American continent and a large part of the Nazca plate - Pacific Ocean while extending sufficiently far away so that no significant deformation is induced at the mesh boundaries. It then goes as deep as the core-mantle boundary, down to 2800 km. Fig. S3 shows different views of the 3D mesh.

Technically, each run takes a time CPU between 8500 and 9500 seconds on a standard desktop computer.

We provide on table S2 the elastic Shear and Bulk moduli as function of depth of the different regions based on the PREM distribution [Dziewonski & Anderson, 1981].

3   COSEISMIC SLIP DISTRIBUTION

We present on fig.S5 the fit to the data of the inverted coseismic slip distribution, in horizontal (c) and vertical (d), together with the subsequent residuals (b). We precise here the origin of data: sGPS stations (grey dots), cGPS stations (white dots) are from [Vigny et al., 2011], black dots for other cited studies ([Delouis et al., 2010], [Tong et al., 2010], [Moreno et al., 2012] and [Lin et al., 2013]).
Our distribution presents a mean horizontal residual of 12 cm and a mean vertical residual of less than 3 cm, maximum residuals are found on GPS benchmarks on the Arauco Peninsula.

Continental (left) and oceanic (right) lithospheres:

Depth (m)	G_{cont}	K_{cont}	G_{ocean}	K_{ocean}
-2.21×10^5	6.56×10^{10}	1.27×10^{11}	6.56×10^{10}	1.27×10^{11}
-60×10^3	68×10^9	130×10^9	68×10^9	130×10^9
-30.1×10^3	68×10^9	130×10^9	68×10^9	130×10^9
-30×10^3	26×10^9	52×10^9	68×10^9	130×10^9
1×10^4	26×10^9	52×10^9	68×10^9	130×10^9

Asthenosphere:

Depth (m)	G	K
-3×10^6	2.94×10^{11}	6.56×10^{11}
-2.89×10^6	2.94×10^{11}	6.56×10^{11}
-1.25×10^6	1.93×10^{11}	3.73×10^{11}
-6.71×10^5	1.55×10^{11}	3×10^{11}
-6.60×10^5	1.25×10^{11}	2.42×10^{11}
-4.06×10^5	9.06×10^{10}	1.76×10^{11}
-4.01×10^5	8.24×10^{10}	1.60×10^{11}
-2.21×10^5	6.56×10^{10}	1.27×10^{11}
-60×10^3	68×10^9	130×10^9

Accretionnary prism:

G	K
20×10^9	40×10^9

Table S2. Shear (G in Pa) and Bulk (K in Pa) moduli as function of depth (PREM).

4   INVERSION OF RHEOLOGICAL PARAMETERS OF A MODEL OF PURE VISCOELASTIC RELAXATION

4.1   Impact of viscoelastic relaxation in the wedge on surface deformation

We explore the possibility of relaxation in a wedge at depth between 50 km and 70 km above the subducting plate, potentially extending beneath the volcanic arc. The effect of this low viscosity wedge, also localized in mid-field, is comparable to that of the shallow channel, although weaker in the horizontal direction but it cannot produce the desired vertical velocity (Fig. S6). Therefore we consider that the existence of such a low viscosity wedge is not supported by the data and exclude it from all the following models.

4.2   Temporal evolution of the VER model over 5 years

Fig.S7 represents the evolution of the model of pure viscoelastic relaxation over 5 years.

4.3 Fit to data in the region of Coquimbo

We provide here a figure highlighting the fit to the data in the region of Coquimbo-La Serena (fig.S8), more than 400 km North of the Maule rupture zone using the model of pure viscoelastic relaxation.

4.4 Impact of viscosity contrast between oceanic and continental asthenosphere

We present here a forward model in which we dissociate the oceanic and continental sides of the asthenosphere (Fig.S9). We attribute a viscosity of 1×10^{20} Pa.s to the oceanic side of asthenosphere, according to [Hu et al.,2004], keeping the inverted value of the asthenosphere of the continental side $(4.75 \times 10^{18}$ Pa.s). We compare this model (represented in green on Fig.S9) to the preferred one (represented in blue) and to the data (represented in red/orange). We can see that in horizontal, the amplitude and the pattern are very similar for both models, except North of the Maule rupture zone (area circled in yellow on Fig.S9-up). There, the model with viscosity contrast predicts Northwestern velocities whereas data show a clear North-East trend that is well predicted by the preferred model. In vertical, the viscosity contrast across the subduction slab affects velocities of coastal stations, reducing the subsidence amplitude (area circled in yellow on Fig.S9-bottom). But the model cannot reproduce the latitude dependence of the sign of the vertical motion observed on GPS data. There is no effect further away, neither on the quick uplift over the Cordillera nor on the large scale subsidence.

Therefore, the viscosity constrat across the subduction slab does not improve the fit to the data. Morover, cGPS stations on oceanic islands away from Sumatra or from Japan present a small but clear postseismic signal after Aceh and Tohoku earthquakes [Trubienko et al., 2014], with an amplitude compatible with a viscosity in the oceanic lithosphere of a few 10×10^{18} Pas. For these two reasons, we do not consider a viscosity contrast in the asthenosphere between the oceanic and continental sides.

5 IMPACT OF VISCOELASTIC RELAXATION VS AFTERSLIP

We provide here the figure of the preferred combined model vs data over the 1st year after the earthquake, together with the afterslip distribution over the same period (fig.S10). Data measured during this first year appear to be more impacted by small and local heterogeneities (such as secondary fault activation, small uncorrected aftershocks). The fit to the data is then logically less good as over the second year, presented on the main article. We also provide a set of GPS time series compared to our preferred model (fig.S11).

Note that tables used in the GPS processing seem to correct only partially offsets due to material changes. For exemple, on the time series LPGS in 2012 (Fig.11 on the main text). The negative offset induced tends to artificially increase the subsidence velocity while the model predicts no significant

vertical motion. A comparable situation is visible in 2012 on the East component of the station CHML (Fig.S11), but there also, the model fits well the time series without considering this artificial offset.

5.1   Correlation of the partial derivatives

Matrix S3 illustrates the correlation among the fields associated with the main parameters inverted for in section 4.4. It represents the normalized covariance matrix computed from the cross correlation of 7 displacement fields computed on the GPS data-points. The first six of these fields correspond to the partial derivatives of the displacement fields with respect to the viscosity in the six regions described in table 1 and the seventh is the displacement due uniquely to the slip on the interface (Fig.S12). Notice the large correlation coefficient between the partial derivatives concerning the deepest and middle part of the channel which indicates that a certain trade-off exists between the viscosities of these two regions. The presence of a very low viscosity in the middle channel (between 70 and 100 km depth) seems however very well constrained. The displacement due to the slip on the interface is also rather poorly correlated with any of the displacement fields associated with partial derivatives with respect to the viscosity. From the inversion of this covariance matrix, one may obtain formal confidence interval for the viscosity coefficients using the classical formulas for errors in least-square estimates.

$$\widehat{se}(\hat{\eta}_j) = \sqrt{s^2(X^TX)^{-1}_{jj}} \tag{1}$$

where $(X^TX)^{-1}_{jj}$ represents the diagonal elements of the inverse of the covariance matrix. $\widehat{se}(\hat{\eta}_j)$ the standard error on the coefficient by which we have to multiply the partial derivative in order to reach the best fit and s^2 the standard error estimated from the residuals of the least-square inversion (found here to be equal to 4.4 mm).

The partial derivatives are computed for an increase of viscosity of 20% (i.e. a variation equal to $log(1.2)$ of the logarithm of the viscosity). From there, one can compute the confidence intervals for each parameter. Those given in table 1 correspond to a confidence level of 90% on the decimal logarithm of the viscosity. The seventh diagonal term of the inverse covariance matrix yields the uncertainty on the coefficient multiplying the slip on the interface, found here to be equal to 2.5%. Note that for simplification purposes, we have decided to include here only one term proportional to the effect of the whole slip on the interface.

	SC1	SC2	DC	LAC	Ast(90-200)	Ast(200-270)	Slip
SC1	1.00	0.547	0.345	0.508	-0.189	-0.256	-0.352
SC2	0.547	1.00	0.927	0.744	0.437	-0.533	1.791e-3
DC	0.345	0.927	1.00	0.819	0.599	-0.566	-6.537e-3
LAC	0.508	0.744	0.819	1.00	0.612	-0.601	-0.311
Ast(90-200)	-0.190	0.436	0.599	0.612	1.00	-0.326	0.138
Ast(200-270)	-0.256	-0.533	-0.566	-0.601	-0.326	1.00	3.519e-2
Slip	-0.352	1.791e-3	-6.537e-3	-0.312	0.138	3.519e-2	1.00

Table S3. Correlation matrix of the viscous parameters inversion

6 IMPACT OF A CRATON IN CENTRAL ARGENTINA

We finally provide the figure of the preferred combined model vs data over the 2nd year after the earthquake, featuring an elastic craton in Central Argentina (fig.S13), which is discussed on section 5.3 of the main paper.
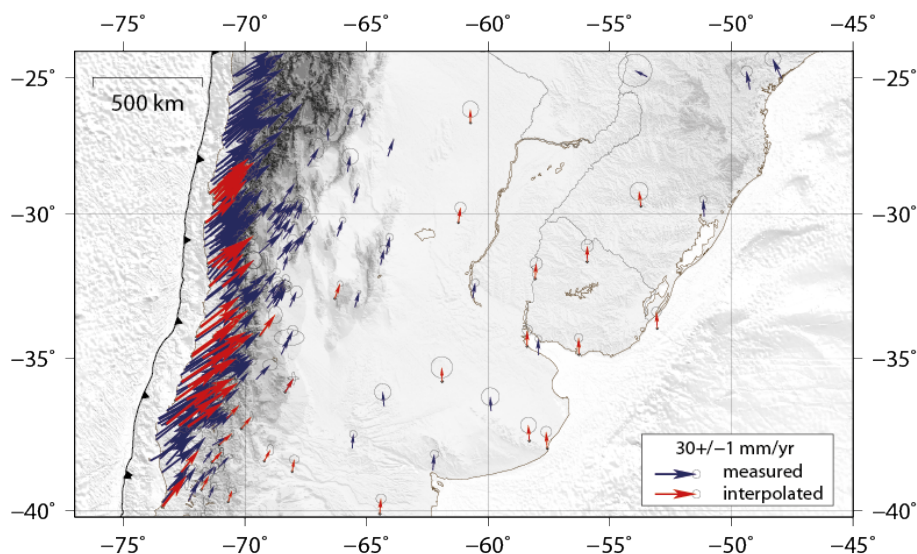
Figure S1. Interseismic velocity field across the whole area expressed in ITRF08 (International Terrestrial Reference Frame). Blue vectors represent the measured velocities, the red ones are interpolated using cubic spline.
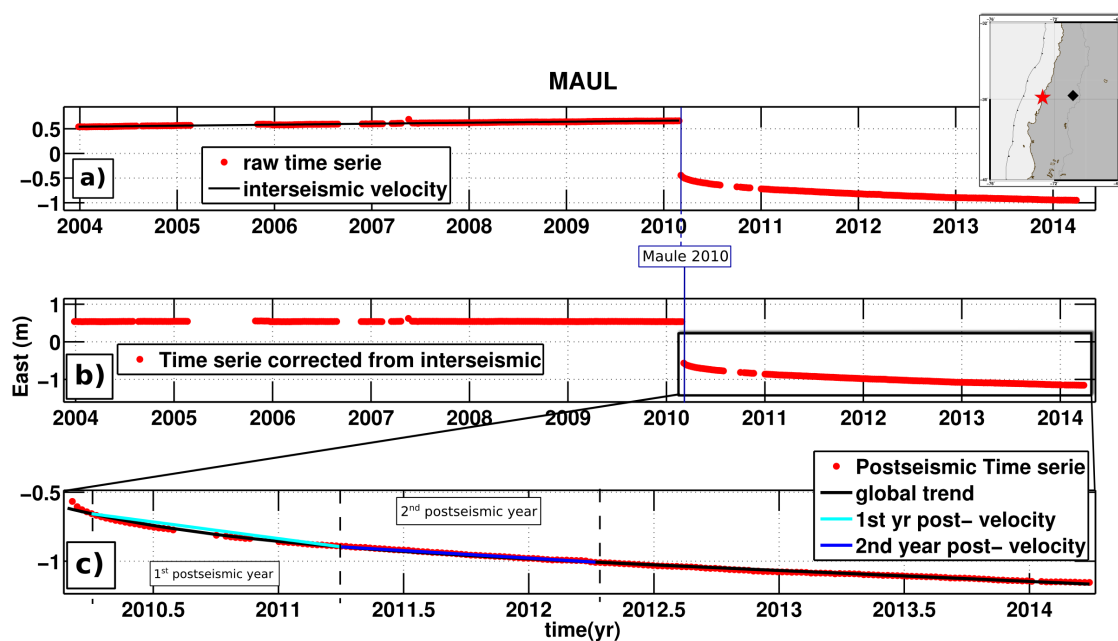
Figure S2. Analysis process of GPS time series, here on the east component of the station of Maule, MAUL, at different stage of the analysis. Insert map shows the location of the station (black diamond) and the Maule earthquake epicenter, from CSN (red star). a) Complete raw time serie. Estimated interseismic velocity is represented by the black line b) Complete time series corrected from the interseismic velocity previously estimated c) Postseismic time series, the global trend is represented in black, annual mean velocities are represented in blue.
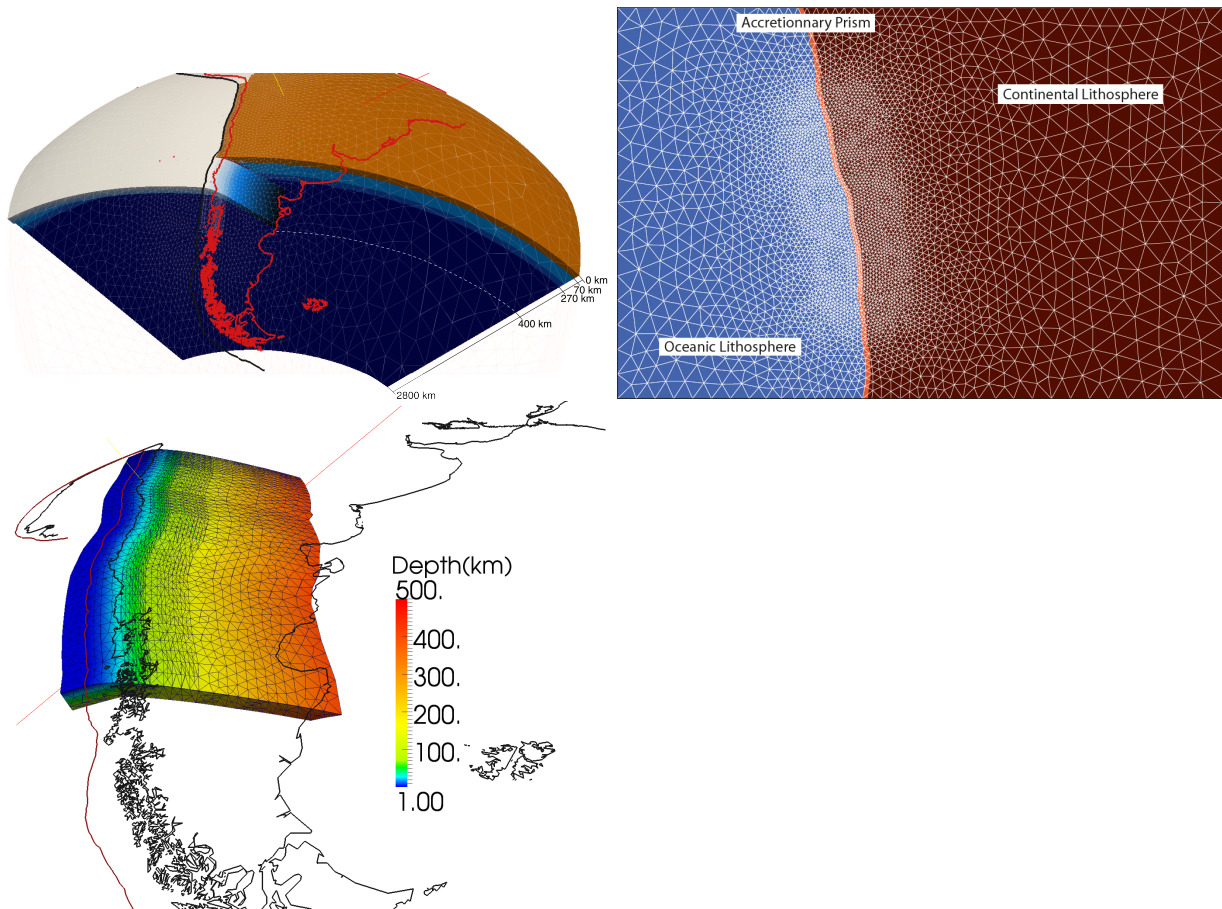
Figure S3. 3D Finite Element mesh featuring a portion of a spherical shell from the core-mantle boundary to the Earth's surface, extending over $60°$ in longitude and latitude. On the right is represented the planar top surface of the mesh, colors defining the different layers and white lines highlight the elements of the mesh. On the bottom is the slab, colors are function of the depth, white lines represent the elements.
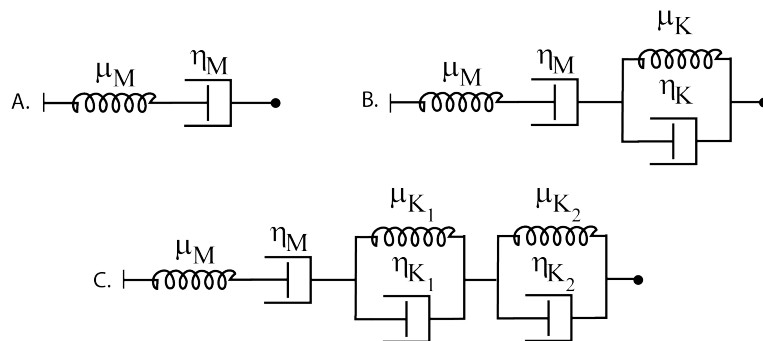
Figure S4. Sketches of the tested rheologies : A. Maxwell rheology; B. Simple Burgers rheology (one Kelvin-Voigt element); C. Complex Burgers with two Kelvin-Voigt elements.
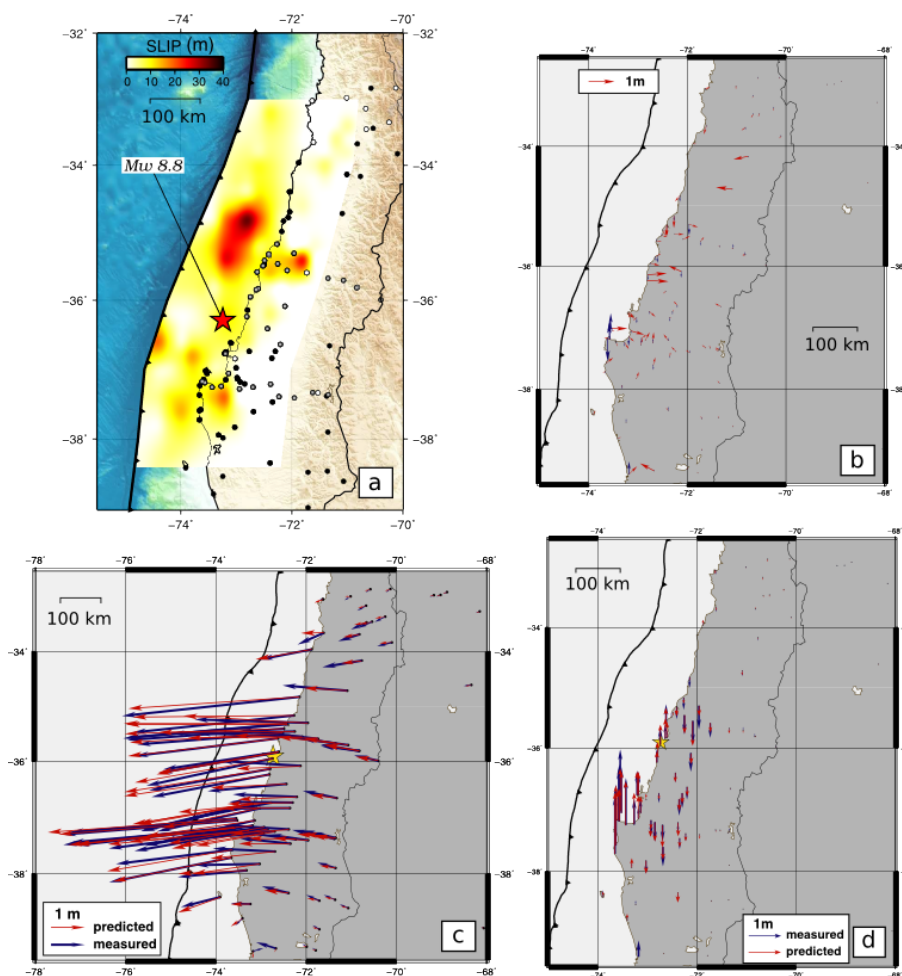
Figure S5. a) Coseismic slip distribution inverted in this study, origin of data are detailed above. The red star depicts the hypocenter (CSN); b) Residuals (Observed vs Computed) in horizontal (red) and in vertical (blue); Observed (blue) vs predicted (red) coseismic displacements (in m) of the earthquake on GPS stations a) in horizontal and b) in vertical.
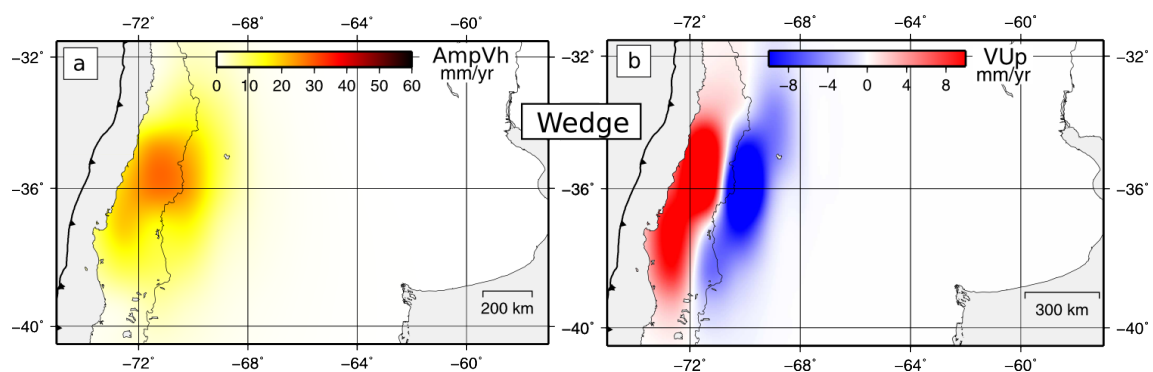
Figure S6. Effect on surface velocities of relaxation in the low viscosity wedge (in addition to figure 5): a) Amplitude of horizontal velocities (Ampl Vh in mm/yr); b) Vertical velocities (Vup in mm/yr).
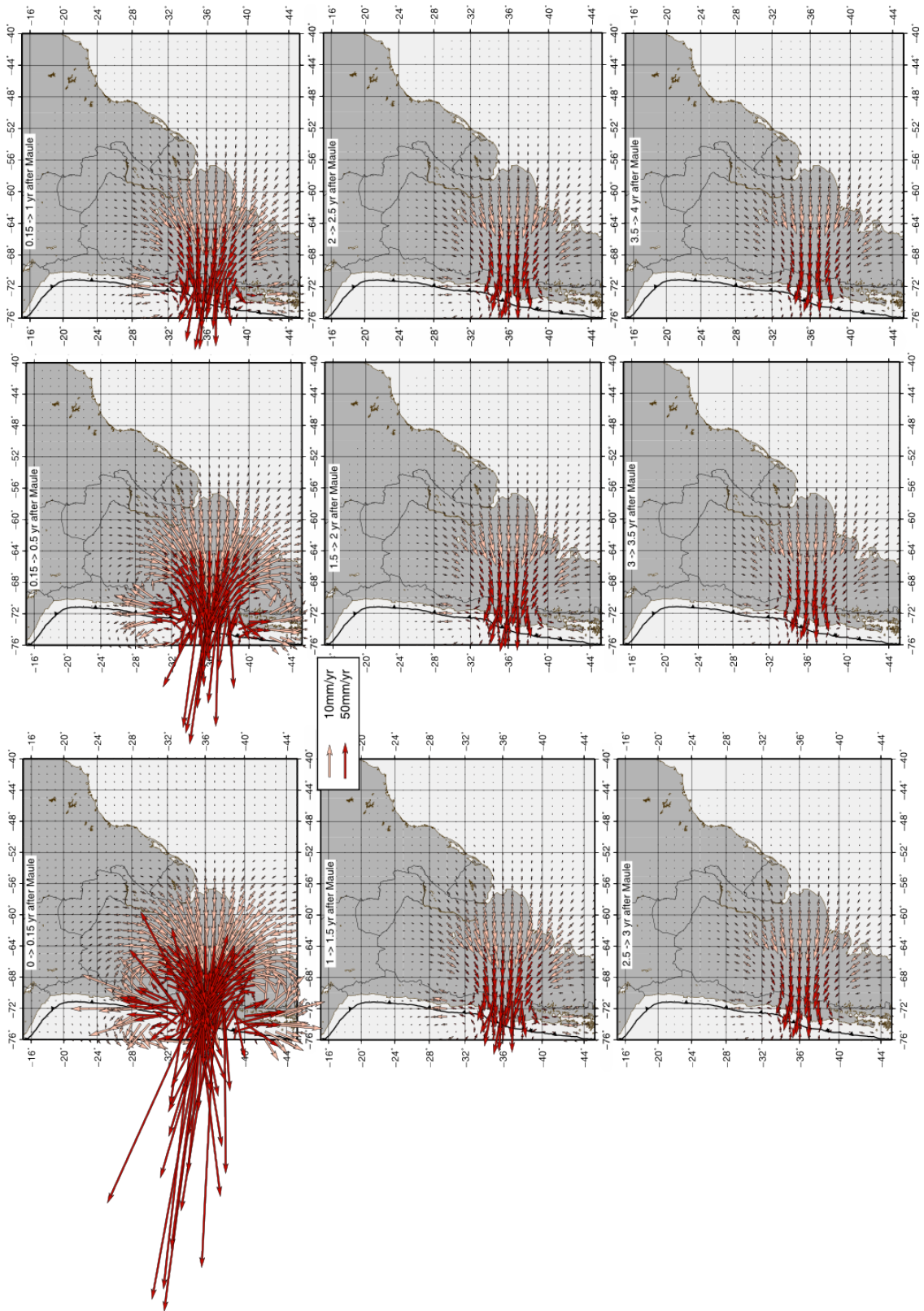
Figure S7. Horizontal evolution as function of time, of the model of pure viscoelastic relaxation on a grid of 1 degre.
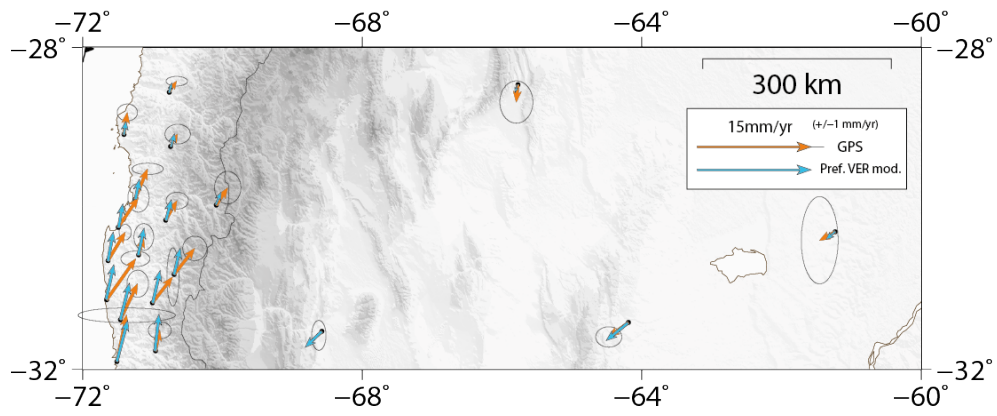
Figure S8. Observed vs predicted mean velocities (mm/yr) between 2011.2 and 2012.2, in the case of the model of pure viscoelastic relaxation in the region of Coquimbo-La Serena (North of the Maulea area)
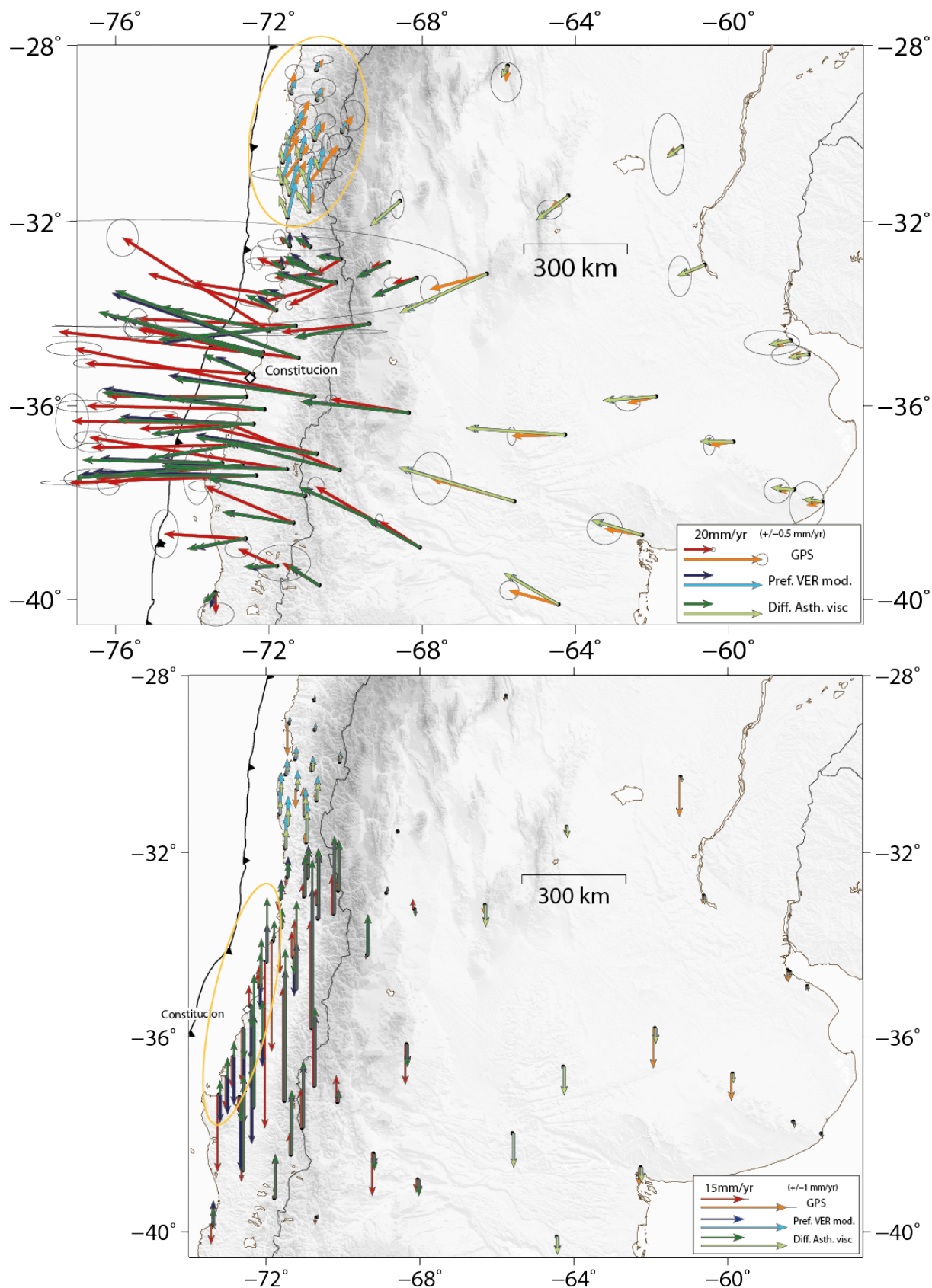
Figure S9. Observed vs predicted mean velocities (mm/yr) between 2011.2 and 2012.2, in the case of 2 models of pure viscoelastic relaxation: the preferred model with undissociated asthenosphere (blue) and a model with different viscosities attributed to the continental (4.75×10^{18} Pa.s - inverted value) and oceanic (1×10^{20} Pa.s) sides of the asthenosphere (green); Horizontal (up), vertical (down).
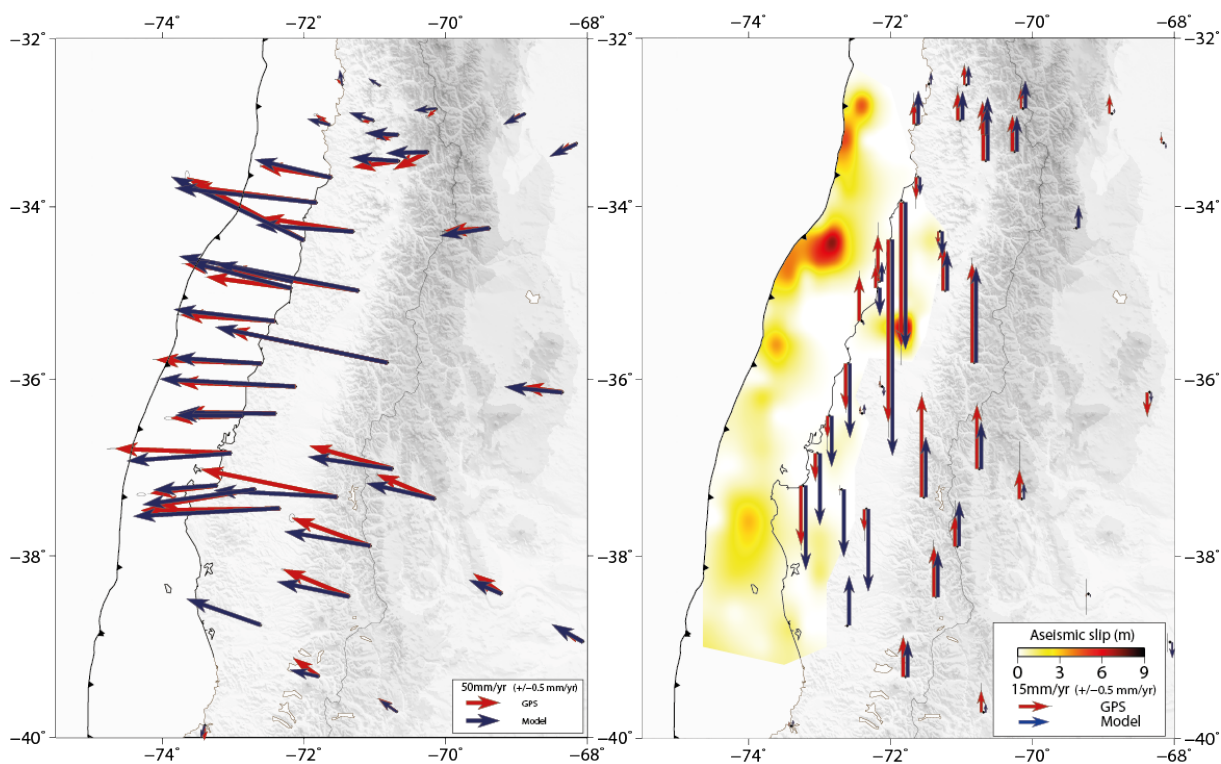
Figure S10. Observed vs predicted mean velocities (mm/yr) between 2010.2 and 2011.2, in the case of the preferred combined model of viscoelastic relaxation and afterslip: left) horizontal velocities, right) vertical velocities. The slip distribution of afterslip is represented in color scale (in m);
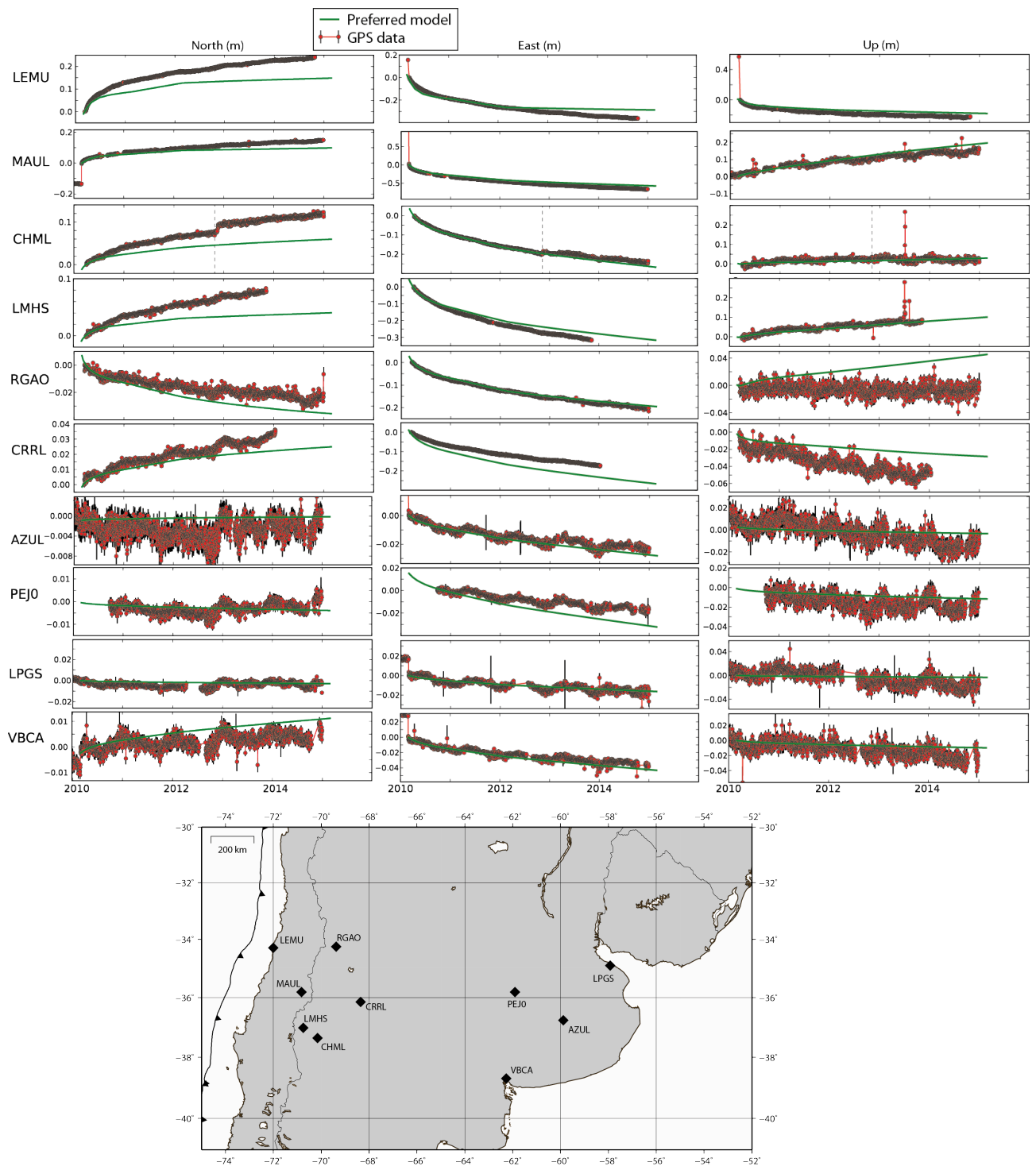
Figure S11. Sample of GPS time series (red) compared to the preferred model of viscoelastic relaxation combined to afterslip (green). Grey dashed lines mark known dates of material changes. Stations are located on the map.
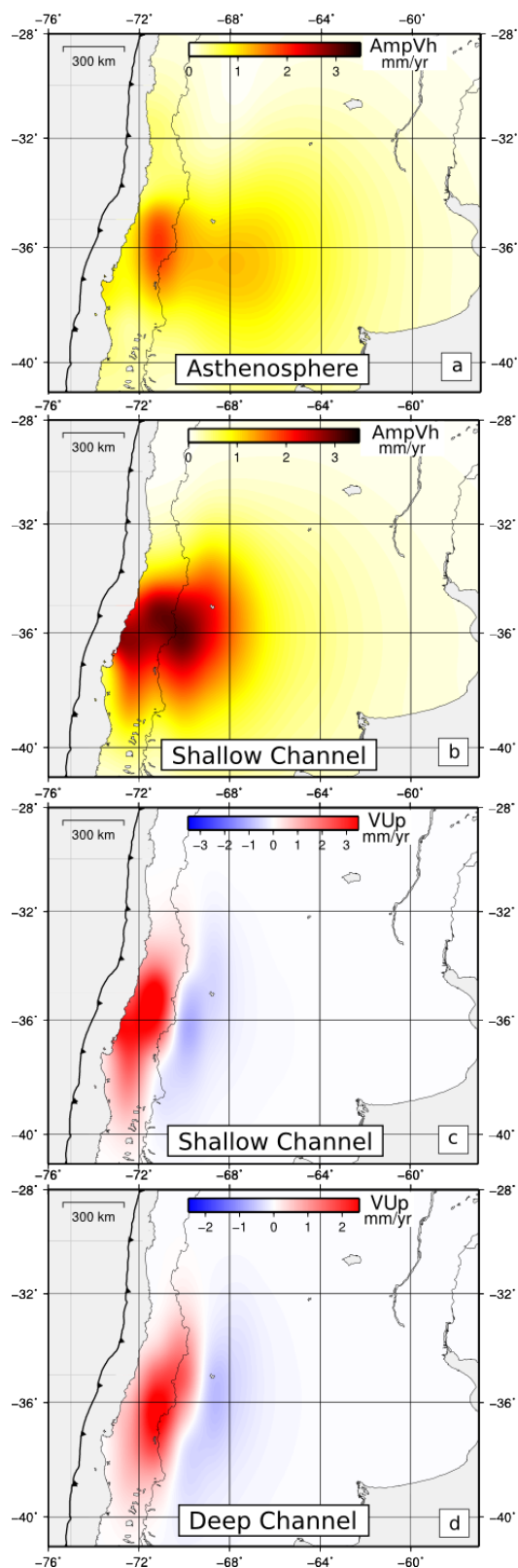
Figure S12. Partial derivative of the computed velocities with respect to the viscosities of the reference model in a) the asthenosphere (amplitude of horizontal velocities mm/yr); b) the shallow channel (amplitude of horizontal velocities mm/yr down to 105 km); c) in the shallow channel (Vertical velocities mm/yr); d) in the deep extention of the deep channel (Vertical velocities mm/yr, down to 135 km).
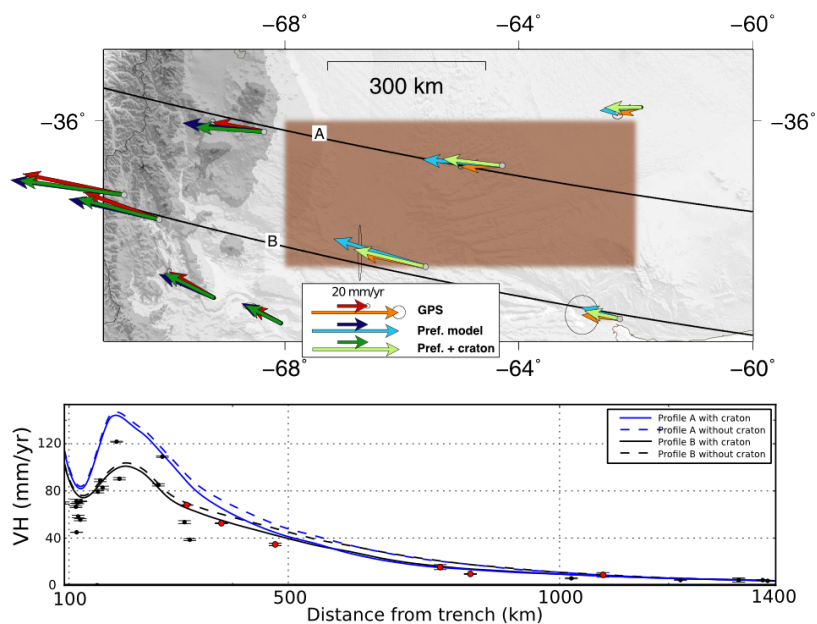
Figure S13. Impact of an elastic craton in central Argentina on horizontal deformation over the 2nd year after the earthquake in surface: top) Zoom over Central Argentina : Observed (red) vs predicted horizontal velocities (mm/yr) of the preferred model without craton (blue) and the same model with a craton (green); bottom) Profile of horizontal velocities (mm/yr) as function of distance from the trench. Dots represent horizontal velocities (mm/yr) measured at GPS stations, red dots are GPS stations located on the map b, around and over the craton along the profiles. The 2 lines represent the models with (solid lines) and without craton (dashed lines), along the profiles A (blue) and B (black).